Phys. Status Solidi A **211,** No. 5, 1155–1161 (2014) / **DOI** 10.1002/pssa.201330394

physica status solidi a
www.pss-a.com
applications and materials science

Mn^{2+}-induced room-temperature ferromagnetism and spin-glass behavior in hydrothermally grown Mn-doped ZnO nanorods

R. Vinod[1], M. Junaid Bushiri*[,1], P. Sajan[1], Sreekumar Rajappan Achary[2], and Vicente Muñoz-Sanjosé[2]

[1] Department of Physics, Cochin University of Science and Technology, Kochi 682022, Kerala, India
[2] Departamento de Fisica Aplicada y Electromagnetismo, Universitat de Valencia, c/Dr. Moliner 50, Burjassot, Valencia 46100, Spain

Received 23 October 2013, revised 10 January 2014, accepted 15 January 2014
Published online 11 February 2014

Keywords diluted magnetic semiconductors, manganese, nanorods, spin glasses, SQUID, ZnO

* Corresponding author: e-mail junaidbushiri@gmail.com, Phone: +91 9495348631, Fax: +91 4842862459

The magnetic properties of Mn-doped ZnO (ZnO:Mn) nanorods grown by hydrothermal process at a temperature of 200 °C and a growth time of 3 h have been studied. The samples were characterized by using powder X-ray diffraction with Rietveld refinement, scanning electron microscopy, energy-dispersive X-ray analysis and SQUID magnetometry. Mn (3 wt%) and (5 wt%)-doped ZnO samples exhibit paramagnetic and ferromagnetic behavior, respectively, at room temperature. The spin-glass behavior is observed from the samples with respect to the decrease of temperature. At 10 K, both samples exhibit a hysteresis loop with relatively low coercivity. The room-temperature ferromagnetism in 5 wt% Mn-doped ZnO nanorods is attributed to the increase in the specific area of grain boundaries, interaction between dopant Mn^{2+} ions substituted at Zn^{2+} site and the interaction between Mn^{2+} ions and Zn^{2+} ions from the ZnO host lattice.

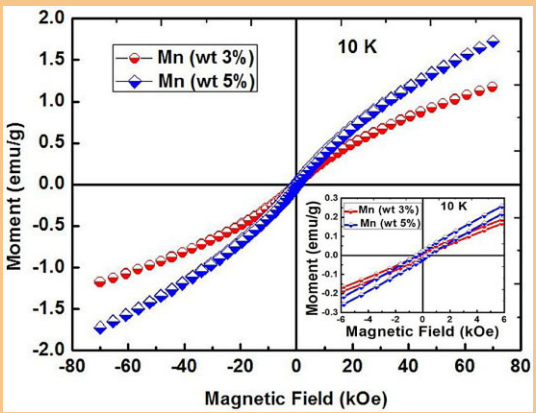

M–H curve of hydrothermally grown ZnO:Mn (3 wt%) and ZnO:Mn (5 wt%) nanorods at 10 K.

1 Introduction Diluted magnetic semiconductors (DMS), which combine ferromagnetism with semiconductivity, are identified to be potential building blocks for spintronic devices [1–3]. Nonmagnetic materials like TiO_2, SnO_2, HfO_2 showed room-temperature ferromagnetism while doping it with a suitable quantity of transition metal elements [4–7]. Prellier et al. [8] reported ferromagnetism in transition metals (TM) doped DMSs with a Curie point above room temperature and are useful for advanced spintronic applications. In particular, in semiconductor materials, ferromagnetism occurs at doping levels far below the percolation threshold and the average magnetic moment per dopant cation progressively increases with decreasing dopant concentration [9]. Zinc oxide (ZnO) is an extensively studied wide direct bandgap (3.37 eV) nontoxic semiconductor with a large exciton binding energy of 60 meV at room temperature [10]. Room-temperature ferromagnetism is theoretically predicted in Mn-doped ZnO (ZnO:Mn) [11]. Following the theoretical prediction that ZnO would become ferromagnetic at room temperature by doping with 3d transition elements, intensive experimental work has been carried out to understand the DMS behavior [12–14]. Manganese is a good transition metal candidate to be used as dopant because of its better thermal solubility (10 mol%) [13]. High-temperature and vapor-phase methods are mostly employed for the fabrication of 1D nanostructures of ZnO:Mn [15]. Mn-doped ZnO

nanowires are also obtained by doping Mn into ZnO by using various techniques, such as ion implantation, thermal evaporation, and wet chemical method [10]. Solution-based synthesis like solvothermal, hydrothermal methods is one of the efficient strategies to prepare Mn-doped ZnO 1D semiconductor nanostructures [16–21]. As stated previously, there are several reports on the magnetic characteristics of ZnO:Mn and inconsistencies exist in these reports [22–24, 26, 27]. A recent first-principles-based study could open new ways to the understanding of the ferromagnetic interactions in this material [25]. Further, it is reported that the specific area of grain boundaries is an important factor that determines the magnetic properties of ZnO as well transition-metal-doped ZnO.

In this context, it requires more experimental and theoretical support to understand the origin of ferromagnetism in ZnO:Mn with different nature like bulk, films and nanostructures, etc. In the present work, we have studied the structure, morphology, and magnetic behavior of ZnO:Mn (3 wt%) and ZnO:Mn (5 wt%) nanorods in order to understand the origin of magnetism of as-synthesized ZnO:Mn nanorods.

2 Experimental ZnO:Mn nanorods were synthesized by the reaction of $Zn(CH_3COO)_2 \cdot 2H_2O$ (0.1 M), $Mn(CH_3COO)_2 \cdot 2H_2O$ (0.1 M), and NaOH (1 M). The initial reactants were dissolved in distilled water and maintained at a pH of about 8–10. The reactants were placed in a sealed Teflon-lined stainless steel autoclave and maintained at a temperature of 200 °C for 3 h under autogenous pressure [17]. After the heating process, the autoclave was allowed to cool naturally to reach room temperature. The resulting precipitate was collected, washed with distilled water, filtered and dried in air atmosphere at room temperature. The X-ray diffraction (XRD) of the samples was obtained by using a Rigaku D/Max-C X-ray diffractometer with Cu Kα radiation ($\lambda = 1.5414$ Å). The powder XRD patterns of samples were processed with the Rietveld refinement method using the FullProf program [28]. X-ray photoelectron spectroscopy (XPS) measurement was carried out by using a Kratos AXIS Ultra spectrometer. The scanning electron microscope (SEM) images and energy-dispersive X-ray analysis (EDX) of the samples were taken using a Hitachi S-4800 SEM. Magnetic properties of the samples were studied with a SQUID magnetometer (QUANTUM DESIGN).

3 Results and discussion

3.1 Structural and compositional characterization Figure 1 shows the Rietveld refined XRD pattern of hydrothermally grown ZnO and ZnO:Mn. The XRD peak shows that the synthesized samples are of good crystallinity. All the diffraction peaks of ZnO and ZnO:Mn nanorods are similar to that of hexagonal wurtzite structure of ZnO (JCPDS: 36-1451) [space group *P63mc* (No. 186)].

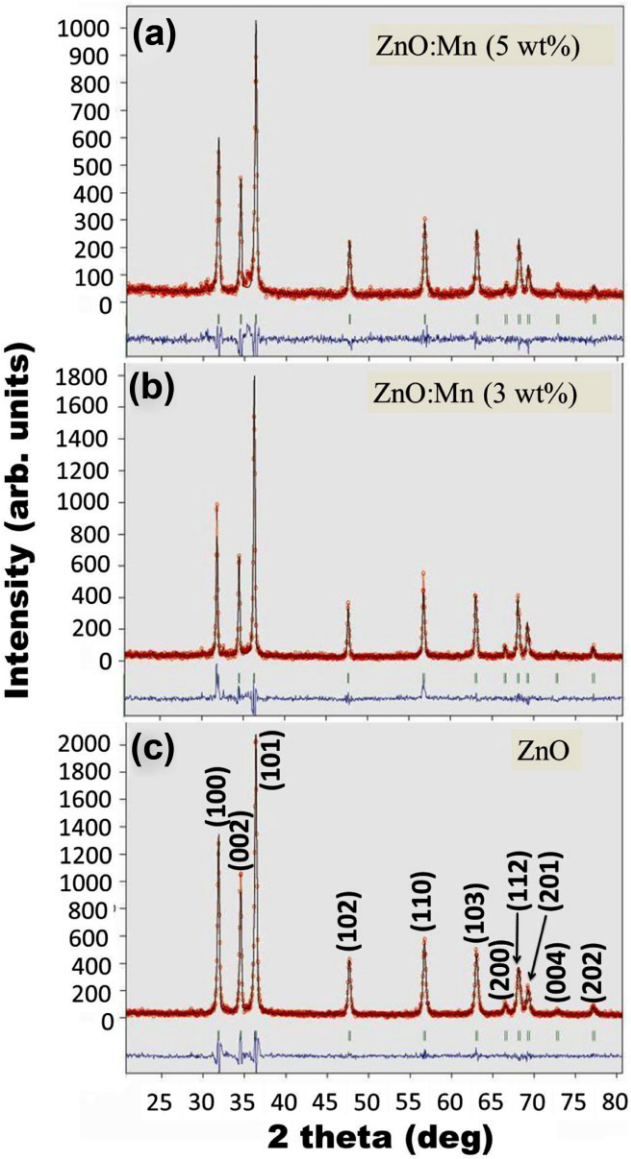

Figure 1 Rietveld refined XRD pattern of hydrothermally grown (a) ZnO:Mn (5 wt%), (b) ZnO:Mn (3 wt%), and (c) ZnO nanorods.

Figure 2 shows the high-resolution XPS Mn-2p spectra of ZnO:Mn nanorods (Mn 3 and 5 wt% doped samples). The Mn-2p peak of ZnO:Mn nanorods is observed at 642.29 eV. This result is in agreement with previously reported binding energy values of the Mn^{2+} ionic state (Mn $2P_{3/2}$) [29]. This indicates the presence of the Mn^{2+} ions in the samples as well as incorporation of Mn^{2+} ions into the ZnO lattice. This observation also confirms the XRD of the present sample, in which there is no additional phase or Mn clusters or crystalline Mn oxides detected. Further, the observed increase of the lattice parameters of Mn-doped ZnO indicates the Mn incorporation into the ZnO lattice/replacement of Mn^{2+} ions in the sites of Zn^{2+} ions. This incorporation of Mn into the ZnO lattice alters the lattice parameters, and

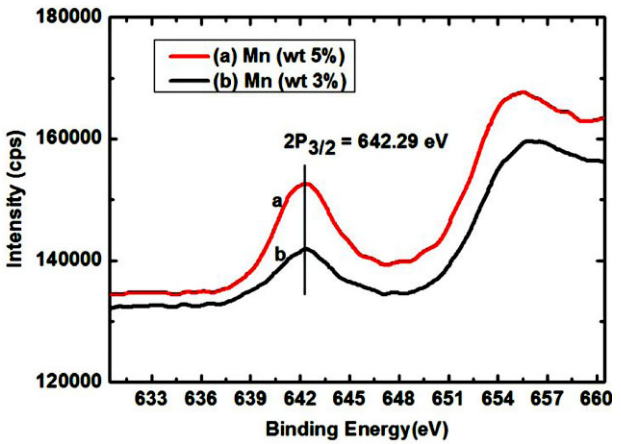

Figure 2 The high-resolution XPS Mn-2p spectra of (a) ZnO:Mn (5 wt%) and (b) ZnO:Mn (3 wt%) nanorods.

induces lattice strain that generates a stress on the host lattice. Nevertheless, the wurtzite structure remains unchanged by the substitution of Mn^{2+} ions by Zn^{2+} ions into the ZnO crystal system. The lattice parameters *a* and *c* of the as synthesized samples are found to be slightly increased with respect to the doping percentage of Mn^{2+} ions (Table 1). The slight variation in calculated lattice constants can be understood if we consider the larger radius of Mn^{2+} ions (0.66 Å) with respect to that of the Zn^{2+} ions (0.60 Å) [30]. The EDX analysis of the samples indicates the incorporation of Mn into the ZnO crystalline system (Table 2).

3.2 Morphological characterization The SEM images recorded from various regions of the sample grown under the same conditions exhibited almost uniform nanorod morphology (Fig. 3). Hydrothermally grown ZnO nanorods are bunched and exhibit flower-like morphology, while ZnO:Mn samples seem to be more or less isolated. ZnO:Mn (3 wt%) nanorods are comparatively larger in size than the ZnO:Mn (5 wt%) sample.

Table 1 Lattice parameters of hydrothermally grown ZnO with the doping concentration of Mn.

lattice constant	standard JCPDS values [36-1451] (in Å)	unit-cell parameters obtained with Rietveld refinement		
		ZnO (in Å)	ZnO:Mn (3 wt%) (in Å)	ZnO:Mn (5 wt %) (in Å)
a	3.2498	3.2455	3.2567	3.2948
c	5.2066	5.1982	5.1997	5.2569

Table 2 EDX analysis result of hydrothermally grown ZnO and ZnO:Mn nanorods.

element	ZnO		ZnO:Mn (3 wt%)			ZnO:Mn (5 wt%)		
	Zn	O	Zn	O	Mn	Zn	O	Mn
wt%	76.23	18.86	72.33	21.20	2.12	67.58	21.07	3.46
at%	42.70	43.19	39.31	47.09	1.37	35.00	44.59	2.13

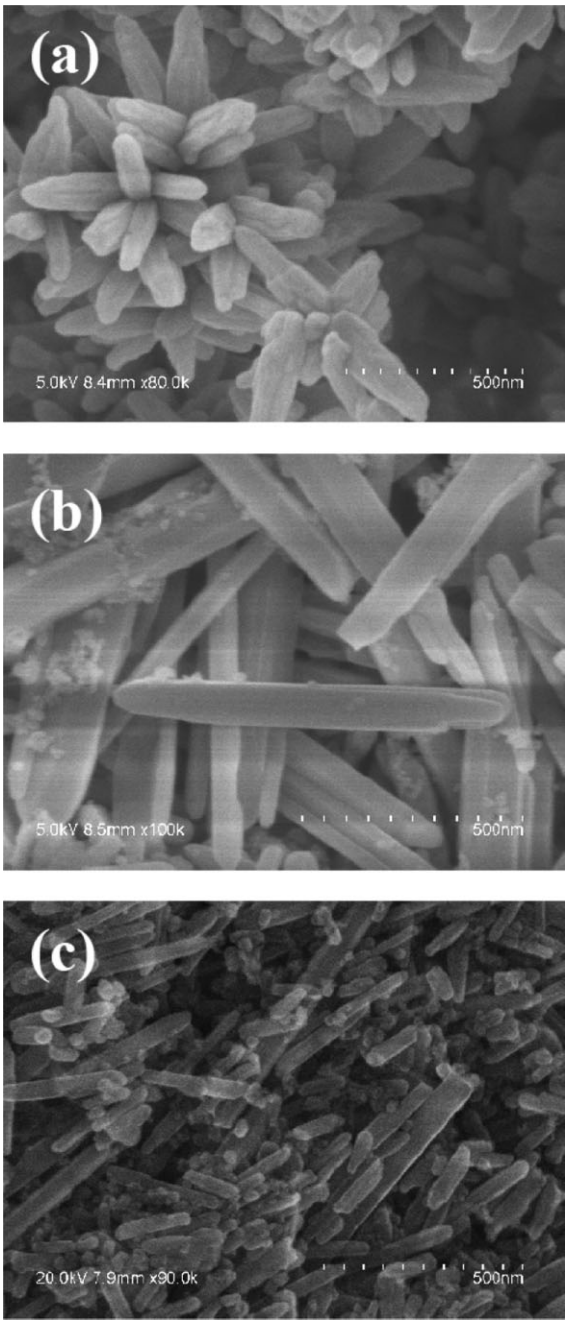

Figure 3 SEM images of hydrothermally grown (a) ZnO, (b) ZnO:Mn (3 wt%) and (c) ZnO:Mn (5 wt%) nanorods.

3.3 Magnetic characterization *M–H* characteristics of hydrothermally grown ZnO nanorods were studied at 10 and 300 K (Fig. 4). These samples exhibit diamagnetic

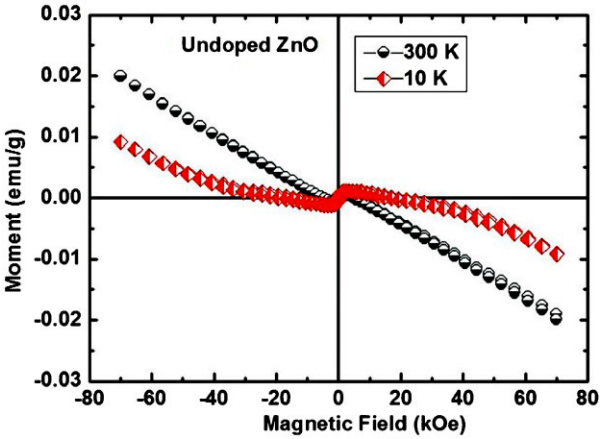

Figure 4 *M–H* curve of hydrothermally grown ZnO nanorods at 10 and 300 K.

nature at both temperatures (10 and 300 K), which is the expected result from the ZnO nanorods. On the other hand, the *M–H* curve at 300 K is almost a straight line without any hysteresis loop for ZnO:Mn (3 wt%) sample (Fig. 5). In the ZnO:Mn (3 wt%) sample, the magnetization reaches a maximum value at an applied field strength of about 69.56 kOe, and showing a magnetic moment of 0.067 emu g^{-1}, and being not saturated. The magnetic susceptibility shows a positive value that indicates the paramagnetic behavior of the material. Interestingly, the ZnO:Mn (5 wt%) sample shows an increase in its magnetic moment as compared to ZnO:Mn (3 wt%) samples at 300 K. The *M–H* curve at 300 K of ZnO:Mn (5 wt%) shows a hysteresis loop with coercivity (H_c) of the order of 0.017 kOe, remanence (M_r) $\sim 1.611 \times 10^{-4}$ emu g^{-1} (Fig. 6). This result indicates that the ZnO:Mn (5 wt%) nanorods exhibit room-temperature ferromagnetic behavior.

On the other hand, at low temperature (10 K; Fig. 7), hysteresis loops with relatively low coercivity were observed

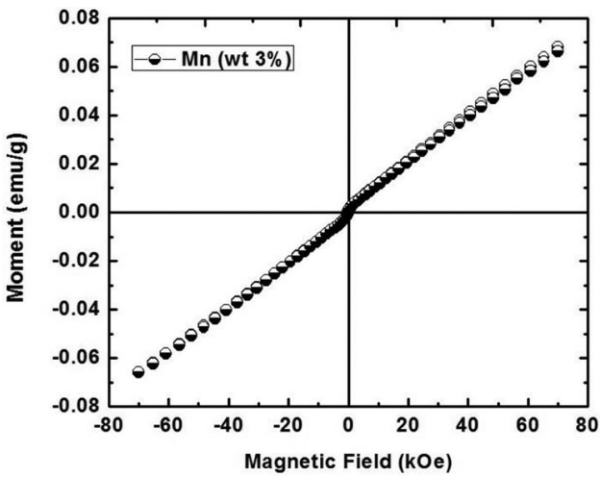

Figure 5 *M–H* curve of hydrothermally grown ZnO:Mn (3 wt%) nanorods at 300 K.

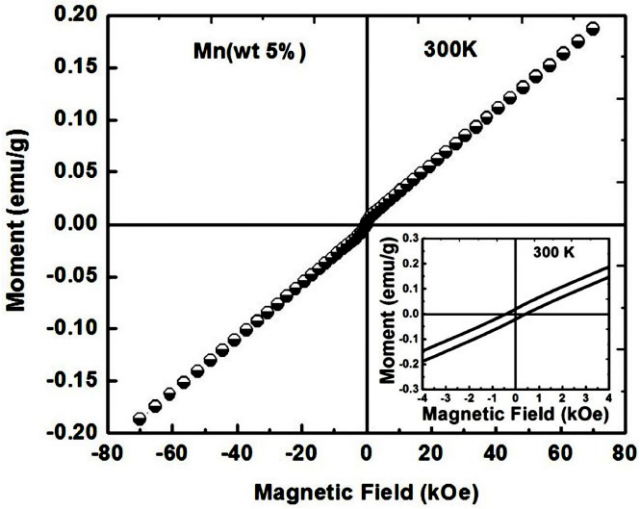

Figure 6 *M–H* curve of hydrothermally grown ZnO:Mn (5 wt%) nanorods at 300 K.

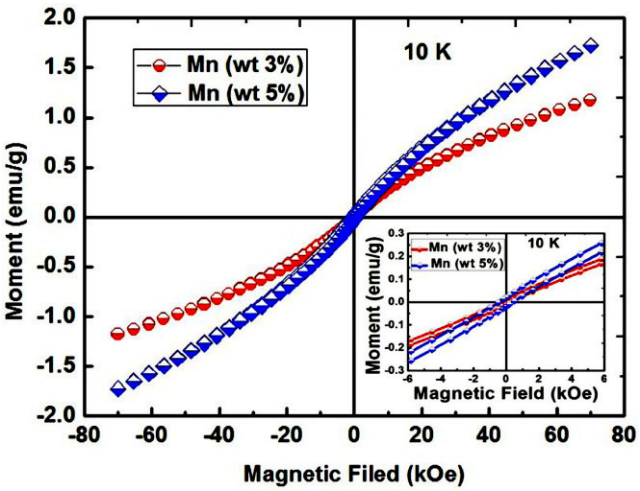

Figure 7 *M–H* curve of hydrothermally grown ZnO:Mn (3 wt%) and ZnO:Mn (5 wt%) nanorods at 10 K.

from all the samples under investigation. ZnO:Mn (3 wt%) samples show coercivity (H_c)$\sim$0.3129 kOe and a remanence value of (M_r) $\sim$ 0.0123 emu g^{-1}. In the ZnO:Mn (5 wt%) sample, coercivity (H_c) is $\sim$ 0.4256 kOe and remanence (M_r) is $\sim$ 0.0205 emu g^{-1}, respectively. Even at this temperature, magnetization is not saturated for all the samples. The hysteresis loop has a nonlinear behavior that shows that the crystalline system is a mixture of paramagnetic and ferromagnetic states.

The temperature dependence of magnetization, under field cooling (FC) with an applied magnetic field of 50 Oe and zero field cooling (ZFC) of ZnO:Mn (3 wt%) nanorods is shown in Fig. 8. The FC and ZFC curves overlap above 47 K and separate from each other below this temperature. Under FC conditions, the magnetization increases slowly

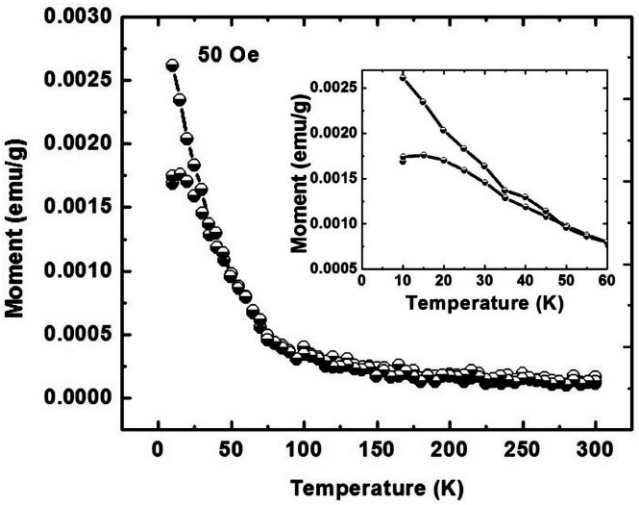

Figure 8 *M–T* plot (FC and ZFC) of hydrothermally grown ZnO:Mn (3 wt%) nanorods at an applied field of 50 Oe. The inset shows the enlarged portion in the low-temperature region.

with decreasing temperature from 300 to 95 K, and then followed by a rapid increase up to 10 K. ZFC is also gradually increased with respect to the decrease of the sample temperature. The FC and ZFC curves overlap in the measuring range of temperatures from 15 to 300 K. The magnitude of the ZFC and FC condition continues to increase without saturation while lowering the temperature, which indicates the presence of diamagnetic ordering in the sample. The magnetization increases slowly with decreasing temperature from 300 to 100 K, followed by a steep increase up to 10 K in the plot of ZnO:Mn (5 wt%) sample (Fig. 9). The figure shows the bifurcation of FC and ZFC at 34 K.

There are different possibilities for the occurrence of ferromagnetism in transition-metal-doped ZnO. Dietl et al. [11] theoretically explained that the room-temperature ferromagnetism in transition-metal-doped ZnO is on the basis of hole doping contributed to the substitution of transition metal in Zn^{2+} sites. The above theoretical explanation is not vivid, because the substitution of the equal valence ions (Mn^{2+} instead of Zn^{2+}) will not create holes. Another model suggests the formation of nanosized Mn_3O_4 with a Curie temperature of 44 K could be a reason for the origin of ferromagnetism in ZnO:Mn [31].

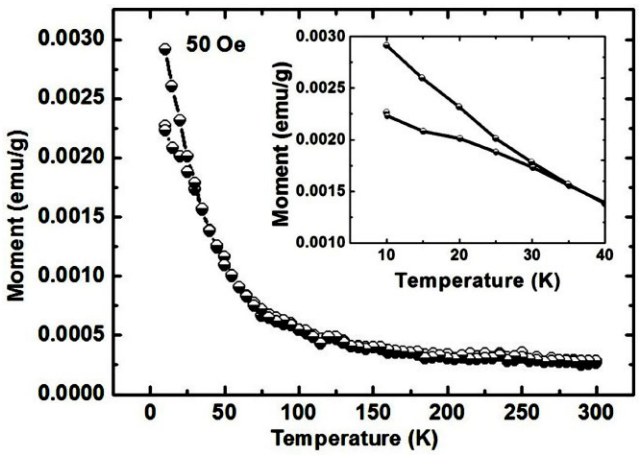

Figure 9 *M–T* plot (FC and ZFC) of hydrothermally grown ZnO:Mn (5 wt%) nanorods at an applied field of 50 Oe. The inset shows the enlarged portion in the low-temperature region.

As described previously, there is no MnO, Mn_3O_4, etc. detected in the ZnO:Mn nanorods synthesized by the hydrothermal process. The observed increase in lattice constants suggest that the substitution of Mn^{2+} ions instead of Zn^{2+} sites rather than the oxide phase of Mn. There will be the possibility to have different types of defects in hydrothermally grown ZnO:Mn nanorods. The native crystal defects like vacancies of O_2 and Zn interstitials on the ZnO host lattice may also generate ferromagnetism in the ZnO nanorods. However, our studies on photoluminescence spectrum of ZnO nanorods even with Mn doping reveal the absence of defect level emission. So there is no possibility for defect-level-activated ferromagnetism to occur in hydrothermally grown ZnO nanorods (Fig. 4). ZnO and transition-metal-doped ZnO samples exhibit ferromagnetic behavior only when the specific area of grain boundaries exceeds a certain threshold value [32]. Straumal et al. [32] reported that a threshold value of specific area of grain boundaries in ZnO is 5.3×10^7 and ZnO:Mn is $2.4 \times 10^5\,m^2\,m^{-3}$. In the case of the present sample, these values are found to be 6.7×10^6, 1.7×10^6, and $10 \times 10^6\,m^2\,m^{-3}$ in ZnO and ZnO:Mn 3 and 5 wt%, respectively. The Mn dopant promotes formation of grain boundaries and the ferromagnetic transition [33]. Further, the solubility of Mn increases with the size of grains and ferromagnetic properties of doped structures are nonmonotonic [32]. The observance of room-temperature ferromagnetism in ZnO:Mn (5 wt%) is attributed to the presence of the increased specific area of grain boundaries and higher solubility of Mn ions in its grains as evidenced by the reduction in diameter of ZnO:Mn (5 wt%) (Fig. 3). From these results, it is inferred that the paramagnetic behavior observed from ZnO:Mn (3 wt%) at 300 K probably due to the reduction of the specific area of grain boundaries as compared to that of ZnO:Mn (5 wt%). Also, an increase in bandgap is observed with the increase in content of Mn into ZnO, the origin of ferromagnetism is also due to Mn doping in the ZnO lattice, which is closely related to the change in bandgap energy of nanorods by the substitution of Mn^{2+} in Zn^{2+} sites [34].

A nonzero difference between the FC and ZFC curves of ZnO:Mn (3 wt%) and ZnO:Mn (5 wt%) indicates the short-range ferromagnetic ordering while decreasing the temperature of the sample, as usually observed in spin-glass systems [35]. This ferromagnetic ordering is further confirmed by the presence of the hysteresis loop at 10 K. The FC and ZFC curves bifurcate each other from a temperature below T_c, indicating the influence of the aging on the spin-

glass state, as was previously reported in $La_{0.95}Sr_{0.05}CoO_3$ and Ag(Mn) spin-glass systems [36, 37].

In the FC–ZFC curve of the ZnO:Mn (5 wt%) sample, the magnetization increases with the decrease in the temperature range of 300–100 K and a rapid increase occurs below 100 K. This behavior is similar to the paramagnetic one. However, this sample shows remanent magnetization and coercivity at room temperature as well. The rapid increase of magnetization at low temperature in ZnO:Mn (5 wt%) can be related to the ferromagnetic properties. Our ZnO sample (Fig. 4) exhibits only diamagnetic behavior at room temperature as well as at 10 K. So, the magnetic properties detected in ZnO:Mn nanorods are due to the interaction between the manganese in the ZnO host lattice, and the detected magnetism point to a superexchange interaction between Mn^{2+} ions and Zn^{2+} ions as well as an increase in specific area of the grain boundaries [38, 32].

One can clearly observe that the ZFC magnetization of both samples does not saturate in the entire measurement range. This is due to the glassy state; the moments are randomly frozen such that it will take a longer time for the field to turn those spins along the field direction [39]. In addition, the FC magnetization is not saturating at low temperature, which indicates the short-range spin ordering in the material [40]. In order to understand the spin-glass ordering, the magnetization irreversibility (M_{irr}) vs. the temperature is plotted. The irreversible magnetization, $M_{irr} = M_{FC} - M_{ZFC}$ as a function of temperature for ZnO:Mn (3 wt%) and ZnO:Mn (5 wt%) nanorods is shown in Fig. 10.

From the graph, one can see that M_{irr} become nonzero at a temperature of 150 K (T_{g1}) for Mn (3 wt%) doped ZnO and that of Mn (5 wt%) doped ZnO is at 140 K (T_{g2}). This temperature is termed as the spin-glass transition temperature (T_g). The spin-glass transition temperature T_{g1} and T_{g2} corresponds to Mn 3 and 5 wt%-doped ZnO, respectively. The M_{irr} is found to rapidly increase and shows a linear behavior from a temperature of about 88 K (T_{cro1}) in Mn (3 wt%)-doped ZnO and 82 K (T_{cro2}) in Mn (5 wt%)-doped ZnO. This temperature is termed as the crossover temperature, as reported by Svedberg et al. [41]. The temperature dependence of M_{irr} in Mn 3 and 5 wt%-doped ZnO is an indication of spin glass ordering attributed to the competing interaction of frozen disorders and magnetic frustrations [42]. However, there are two regimes that can be observed in the graph representing the temperature-dependent irreversibility of magnetization for the spin-glass ordering of the present sample (Fig. 10). The first one is between the T_g and T_{cro} of each sample for which the rate of variation remains small. But below T_{cro}, a rapid, roughly linear increase is determined in both the samples. The linear upward curve seen in the low temperature region suggests that the spin-glass transition observed in the present sample is similar to that of the Ising model predicted by De Almeida-Thouless [43, 44].

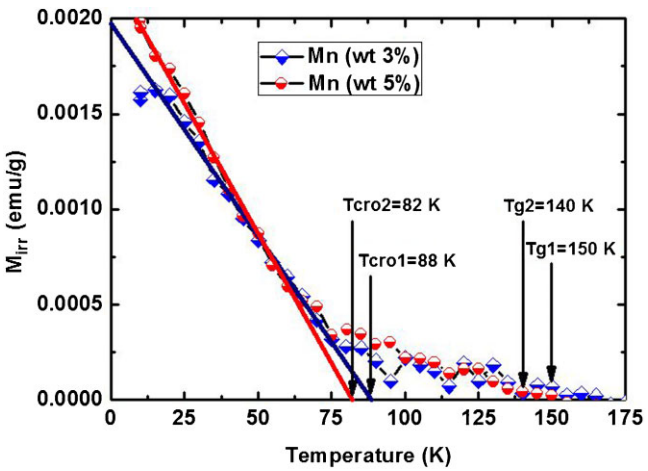

Figure 10 Temperature-dependent irreversibility magnetization $M_{irr} = M_{FC} - M_{ZFC}$ of ZnO:Mn (3 wt%) and ZnO:Mn (5 wt%) nanorods.

4 Summary and conclusions Hydrothermally grown ZnO retains the rod-like morphology with low percentage of Mn doping. The magnetic behavior of ZnO:Mn nanorods depends on the doping percentage of Mn into the ZnO lattice. Hydrothermally grown ZnO nanorods exhibit a diamagnetic nature at 10 and 300 K. At room temperature (300 K), ferromagnetism is observed in ZnO:Mn (5 wt%) nanorods, while ZnO:Mn (3 wt%) nanorods show paramagnetism. The ZnO:Mn (3 wt%) and ZnO:Mn (5 wt%) nanorods exhibit spin-glass behavior below 150 and 140 K, respectively. The variation of magnetic behavior with respect to the level of Mn doping can be attributed to the population of Mn^{2+} ions in the ZnO crystalline lattice. The interaction between doped Mn^{2+} ions and the substitution of Mn^{2+} ions into Zn^{2+} sites and the increase in specific area of the grain boundaries are a contributing factor for the origin of the magnetic behavior. ZnO:Mn nanorods synthesized by a low-temperature hydrothermal process at a reduced reaction time could be used as a potential material for the fabrication of versatile functional spintronic devices.

Acknowledgements R. Vinod acknowledges the University Grants Commission, Government of India for Rajiv Gandhi National Fellowship. The fruitful discussion with Hysen Thomas, Department of Physics, CUSAT about Rietveld analysis is acknowledged. The authors acknowledge funding received from the Ministry of Science and Technology, Spain, TEC 2011-28076, PIB2010JP-00279, and Generalitat Valenciana through the projects Prometeo/2011-035 and ISIC/2012/008 (Institute of Nanotechnologies for Clean Energies of the Generalitat Valenciana). The authors would like to acknowledge Dr. Senoy Thomas, the Chemnitz University of Technology, Germany for SQUID-VSM measurements.

References

[1] J. K. Furdyna, J. Appl. Phys. **64**, R29 (1988).
[2] X. B. He, T. Z. Yang, J. M. Cai, C. D. Zhang, H. M. Guo, D. X. Shi, and C. D. Shen, and H. J. Gao, Chin. Phys. B **17**, 3444 (2008).

[3] K. H. Zheng, Z. Liu, J. Liu, L. J. Hu, D. W. Wang, C. Y. Chen, and L. F. Sun, Chin. Phys. B **19**, 026101 (2010).
[4] K. Ueda, H. Tabata, and T. Kawai, Appl. Phys. Lett. **79**, 988 (2001).
[5] M. Yuji, M. Makoto, S. Tomoji, H. Tetsuya, F. Tomoteru, K. Masashi, A. Parhat, C. Toyohiri, Y. S. Shin, and K. Hideomi, Science **291**, 854 (2001).
[6] S. B. Ogale, R. J. Choudhary, J. P. Buban, S. E. Lofland, S. R. Shinde, S. N. Kale, V. N. Kulkarni, J. Higgins, C. Lanci, J. R. Simpson, N. D. Browning, S. S. Das, H. D. Drew, R. L. Greene, and T. Venkatesan, Phys. Rev. Lett. **91**, 077205 (2003).
[7] N. H. Hong, J. Sakai, N. Poirot, and A. Ruyter, Appl. Phys. Lett. **86**, 242505 (2005).
[8] W. Prellier, A. Foucheta, and B. Mercey, J. Phys.: Condens. Matter. **15**, R1583 (2003).
[9] J. M. D. Coey, M. Venkatesan, and C. B. Fitzgerald, Nature Mater. **4**, 173 (2005).
[10] U. Ozgur, Y. I. Alivov, C. Liu, A. Teke, M. A. Reshchikov, S. Dogan, V. Avrutin, S. J. Cho, and H. Morkoc, J. Appl. Phys. **98**, 041301 (2005).
[11] S. Dietl, H. Ohno, F. Matsujura, J. Cibert, and D. Ferrand, Science **287**, 1019 (2000).
[12] X. Y. Zhang, J. Y. Dai, and H. C. Ong, Open J. Phys. Chem. **1**, 6 (2011).
[13] P. Sharma, A. Gupta, K. V. Rao, F. J. Owens, R. Sharma, R. Ahuja, G. J. M. Osorio, B. Johansson, and G. A. Gehring, Nature Mater. **2**, 673 (2003).
[14] K. Sato and Y. H. Katayama, Physica E **10**, 251 (2001).
[15] Y. Q. Chang, D. B. Wang, X. H. Luo, X. Y. Xu, X. H. Chen, L. Li, C. P. Chen, R. M. Wang, J. Xu, and D. P. Yu, Appl. Phys. Lett. **83**, 4020 (2003).
[16] L. Jin, F. Huiqing, C. Xiaopeng, and C. Zhiyi, Colloids Surfaces A **349**, 202 (2009).
[17] R. Vinod, P. Sajan, R. A. Sreekumar, M. T. Carmen, M. S. Vicente, and M. J. Bushiri, J. Phys. D, Appl. Phys. **45**, 425103 (2012).
[18] Y. Zhang, J. Q. Xu, Q. Xiang, H. Li, Q. Pan, and P. Xu, J. Phys. Chem. C **113**, 3430 (2009).
[19] L. Vayssieres, Adv. Mater. **15**, 464 (2003).
[20] J. X. Wang, X. W. Sun, Y. Yang, H. Huang, Y. C. Lee, O. K. Tan, and L. Vayssieres, Nanotechnology **17**, 4995 (2006).
[21] L. E. Greene, M. Law, J. Goldberger, F. Kim, J. C. Johnson, Y. F. Zhang, R. J. Saykally, and P. D. Yang, Angew. Chem. Int. Ed. **42**, 3031 (2003).
[22] Y. Guo, X. Cao, X. Lan, C. Zhao, X. Xue, and Y. Song, J. Phys. Chem. C **112**, 8832 (2008).
[23] D. A. Schwartz and D. R. Gamelin, Adv. Mater. **16**, 2115 (2004).
[24] N. H. Hong, N. Poirot, and J. Sakai, Appl. Phys. Lett. **89**, 042503 (2006).
[25] M. H. F. Sluiter, Y. Kawazoe, P. Sharma, A. Inoue, A. R. Raju, C. Rout, and U. V. Waghmare, Phys. Rev. Lett. **94**, 187204 (2005).
[26] Y. B. Lin, J. P. Xu, W. Q. Zou, L. Y. Lv, Z. H. Lu, F. M. Zhang, Y. W. Du, Z. G. Huang, and J. G. Zheng, J. Phys. D, Appl. Phys. **40**, 3674 (2007).
[27] J. H. Li, D. Z. Shen, J. Y. Zhang, D. X. Zhao, B. S. Li, Y. M. Lu, Y. C. Liu, and X. W. Fan, J. Magn. Magn. Mater. **302**, 118 (2006).
[28] J. Rodriguez-Carvajal, Fullprof: A program for Rietveld Refinement and Profile Matching Analysis of Complex Powder Diffraction Patterns ILL.
[29] B. Zhang, M. Li, J. Z. Wang, L. Q. Shi, and H. S. Cheng, Mater. Sci. Appl. **4**, 307 (2013).
[30] D. Igor, G. George, A. Denis, P. Matej, J. Zvonko, and N. Markus, J. Mater. Chem. **18**, 5208 (2008).
[31] Y. Q. Chang, D. B. Wang, X. H. Luo, X. Y. Xu, X. H. Chen, R. M. Wang, J. Xu, and D. P. Yu, Appl. Phys. Lett. **83**, 4020 (2003).
[32] B. B. Straumal, S. G. Protasova, A. A. Mazilkin, G. Schütz, E. Goering, B. Baretzky, and P. B. Straumal, JETP Lett. **97**, 415 (2013).
[33] B. B. Straumal, A. A. Mazilkin, S. G. Protasova, P. B. Straumal, A. A. Myatiev, G. Schütz, E. J. Goering, T. Tietze, and B. Baretzky, Philos. Mag. **93**, 1371 (2013).
[34] S. W. Jung, S.-J. An, J. C. Yi, C. U. Jung, S.-I. Lee, and S. Cho, Appl. Phys. Lett. **80**, 4561 (2002).
[35] J. Young,-II F. C. Chou, and Y. M. Chiang, Appl. Phys. Lett. **74**, 2504 (1999).
[36] D. N. H. Nam, R. Mathieu, P. Nordblad, N. V. Khiem, and N. X. Phuc, Phys. Rev. B **62**, 8989 (2000).
[37] R. Mathieu, P. Jonsson, D. N. H. Nam, and P. Nordblad, Phys. Rev. B **63**, 092401 (2001).
[38] T. Nidhi, M. Y. Seikh, and V. Y. Jatinder, Phys. Chem. Chem. Phys. **12**, 12208 (2010).
[39] C. Tien, C. H. Feng, C. S. Wur, and J. J. Lu, Phys. Rev. B **61**, 1251 (2000).
[40] S. L. Young, H. Z. Chen, L. Hong, J. B. Shi, and Y. C. Chen, Jpn. J. Appl. Phys. **40**, 4878 (2001).
[41] M. Svedberg, S. Majumdar, H. Huhtinen, P. Paturi, and S. Granroth, J. Phys.: Condens. Matter **23**, 386005 (2011).
[42] M. Gruyters, Phys. Rev. Lett. **95**, 077204 (2005).
[43] F. Lefloch, J. Hammann, M. Ocio, and E. Vincent, Physica B **203**, 63 (1994).
[44] J. R. L. De Almeida and D. J. Thouless, J. Phys. A **11**, 983 (1978).